1   REVISION 1

2   Word count: 8375

3   **Trace element segregation to dislocation loops in experimentally**

4   **heated zircon**

5   Emily M. Peterman[1]*, Steven M. Reddy[2,3], David W. Saxey[3], Denis Fougerouse[2,3], M. Zakaria

6   Quadir[4], Michael J. Jercinovic[5]

7   [1] Department of Earth & Oceanographic Science, Bowdoin College, Brunswick, ME 04011,

8   USA

9   [2] School of Earth and Planetary Sciences, Curtin University, Perth, Western Australia, AUS

10   [3] Geoscience Atom Probe, John de Laeter Centre, Curtin University, Perth, Western Australia,

11   AUS

12   [4] Microscopy and Microanalysis Facility, John de Laeter Centre, Curtin University, Perth,

13   Western Australia, AUS

14   [5] Department of Geosciences, University of Massachusetts, Amherst, MA 01003

15   *Corresponding author emily.peterman@bowdoin.edu

16

17   **Abstract**

18   To evaluate the mechanisms driving nanoscale trace element mobility in radiation damaged

19   zircon, we analyzed two well-characterized Archean zircons from the Kaapvaal craton (southern

20   Africa): one zircon remained untreated and the other was experimentally heated in the laboratory

21   at 1450°C for 24h. Atom probe tomography (APT) of the untreated zircon reveals

22   homogeneously distributed trace elements. In contrast, APT of the experimentally heated zircon

23   shows that Y, Mg, Al, Pb + Yb segregate to a set of two morphologically and

24   crystallographically distinct cluster populations that range from 5 nm tori to 25 nm toroidal

25   polyhedra, which are confirmed to be dislocation loops by transmission electron microscopy

26   (TEM). The dislocation loops lie in {100} and {001} planes; the edges are aligned with {100},

27   {101}, and {001}. The largest loops (up to 25 nm diameter) are located in {100} and

28   characterized by high concentrations of Mg and Al, which are aligned with <001>. The

29    $^{207}Pb/^{206}Pb$ measured from Pb atoms located within all of the loops (0.264 ± 0.025; 1σ) is

30   consistent with present-day segregation and confirms that the dislocation loops formed during

31   our experimental treatment. These experimentally-induced loops are similar to clusters observed

32   in zircon affected by natural geologic processes. We interpret that differences in cluster

33   distribution, density, and composition between experimentally heated and geologically affected

34   zircon are a function of the radiation dose, the pressure-temperature-time history, and the

35   original composition of the zircon. These findings provide a framework for interpreting the

36   significance of clustered trace elements and their isotopic characteristics in zircon. Our findings

37   also suggest that the processes driving cluster formation in zircon can be replicated under

38   laboratory conditions over human timescales, which may have practical implications for the

39   mineralogical entrapment of significant nuclear elements.

40

41   Keywords: zircon, radiation damage, APT, TEM, dislocation loop, annealing

42

43   **Introduction**

44   Zircon ($ZrSiO_4$) is commonly used across the geosciences to determine the timing and tempo of

45   geologic events because it is chemically and physically robust, it incorporates U (and Th) during

46   crystallization whilst excluding Pb, and trace element characteristics within the grain can be

47   correlated with conditions of growth and recrystallization (e.g., Rubatto, 2002; Hoskin and

48   Schaltegger, 2003). When subjected to changes in pressure (P), temperature (T), and/or fluids,

49   zircon can anneal and/or recrystallize (Nasdala et al., 2001; 2002; Geisler, 2002), which can

50   potentially redistribute trace elements within the crystal (Rubatto, 2002; Geisler et al., 2007;

51   Harley et al., 2007).

52

53   One of the correlative factors associated with the mobility of trace elements in zircon is the

54   accumulated radiation damage (Murakami et al., 1991; Meldrum et al., 1998; Cherniak and

55   Watson, 2003; Ewing et al., 2003). In recent years, quantitative analyses of zircon by atom probe

56   tomography have revealed heterogeneous distributions of trace elements at the nanoscale.

57   Examples include: Pb + Y + Al diffusion to radiation damaged sites (Valley et al., 2014; 2015),

58   pipe diffusion of Pb along dislocation arrays into metamict domains within zircon (Piazolo et al.,

59   2016), diffusive transport of trace elements to deformation microstructures (Piazolo et al., 2016;

60   Reddy et al., 2016; Montalvo et al., 2019), and Pb + Y migration and entrapment within

61   dislocation loops during prograde metamorphism (Peterman et al., 2016; 2019). These findings

62   suggest that trace elements, including Pb, can be mobilized to discrete sites in radiation damaged

63   zircon, consistent with results from ion imaging (Kusiak et al., 2013; Ge et al., 2018). However,

64   each of these studies were carried out on metamorphosed natural zircon specimens that record

65   complex geologic and thermal histories. As a result, the details of the interpreted mechanisms of

66   trace element mobility are difficult to unravel in these complex samples.

67

68   Here, we evaluate the relationships among radiation damage, recrystallization, and trace element

69   mobility in zircon by integrating scanning electron microscopy (SEM), atom probe tomography

3

70 (APT), and transmission electron microscopy (TEM) to analyze an experimentally-heated

71 Archean zircon with a well-characterized and simple thermal history. We compare our findings

72 with results from an untreated zircon from the same sample. Our objectives are to evaluate if

73 short duration, high-temperature (1450°C for 24h) heating produces new nanoscale defects and,

74 if so, whether these features exhibit similar trace element characteristics to those observed in

75 natural zircon affected by geologic processes. Because the zircon originally crystallized in the

76 Archean eon, sufficient quantities of both radiogenic Pb isotopes should have accumulated,

77 enabling the calculation of $^{207}Pb/^{206}Pb$ dates and the quantification of the timing of trace element

78 migration. By comparing these nanoscale datasets, we aim to elucidate the primary drivers of

79 trace element mobility and segregation in zircon, the crystallographic control on the distribution

80 of these clusters, and the possible implications for treatment of materials used for nuclear

81 storage.

82

83 **Sample description**

84 This study examined euhedral zircon extracted from an Archean granitoid (sample SA16-24

85 from -26.045497, 31.428056; Baughman and Flowers, 2020) within the Southeastern Kaapvaal

86 craton, southern Africa. From the Archean through the Phanerozoic eons, the Kaapvaal craton

87 was involved in a series of terrane accretions and orogenic events, including the Namaqua-Natal

88 orogenesis, the assembly of Rodinia, and the assembly and breakup of Pangea (e.g., de Wit et al.

89 1992; Baughman and Flowers, 2020). The Kaapvaal craton was initially stabilized in the

90 Archean eon (3.6 to 3.0 Ga) and cooled to <300°C by 2.7 Ga, as constrained by U-Pb titanite and

91 apatite geochronology (Schoene and Bowring, 2006) and $^{40}Ar/^{39}Ar$ biotite thermochronology

92 (Layer et al., 1992). The crystallization age of the studied granitoid has been best constrained by

93   analyses of 15 air-abraded zircon grains from a nearby granitoid of the same gneiss complex,

94   which yield a mean age of 3.13 ± 0.06 Ga (1σ) (AGC01-4; Schoene and Bowring, 2006). The

95   post-crystallization thermal history of the studied granitoid as constrained by (U-Th)/He zircon

96   analysis includes a low-temperature event (150–250°C) between 1.2 and 1.0 Ga and burial at up

97   to 160°C c. 200 Ma ago (Baughman and Flowers, 2020).

98

99   **Methods**

100   Five euhedral zircon grains ~350 x 150 µm were air-annealed in a covered Pt crucible at 1450°C

101   for 24h in a Deltech furnace at Stanford University. The temperature was increased at 400°C/h

102   until reaching the 1450°C set point. A representative grain from this aliquot was selected for

103   APT analysis and mounted in a 1" (2.54 cm) epoxy round along with representative zircon grains

104   that were untreated. The mount was progressively polished to expose the interior. Following a 1

105   µm polishing step, the mount was affixed to a halved brass rod and polished with colloidal silica

106   for 3h on a Buehler Vibromet2 vibratory polisher. The mount was thoroughly rinsed with water

107   and ethanol and dried in a desiccator overnight. A 10 nm carbon coat was evaporated onto the

108   mount to minimize charging during imaging. Secondary electron and cathodoluminescence (CL)

109   images (**Fig. 1**) were collected on the Tescan Vega3 SEM at Bowdoin College operated at 14

110   kV, 0.3 to 1 nA. Post-APT and post-TEM CL images were acquired on the Tescan CLARA field

111   emission SEM at Curtin University using a 10 kV, 300 pA beam.

112

113   Crystallographic orientations were measured using an Oxford Instruments NordlysMax[3] electron

114   backscatter diffraction (EBSD) system attached to the Tescan Vega3 SEM at Bowdoin College.

115   The SEM was operated at 20 kV, 10 nA at a working distance of 25 mm, with the mount tilted

116   70° toward the EBSD detector. EBSD data were acquired with Oxford Instruments AZtec 3.4

117   software. Acquisition settings were 4 x 4 binning, gain = 7, Hough resolution = 60, 7 bands.

118   Lattice parameters for the zircon match unit were from Hazen and Finger (1979); the measured

119   mean angular deviations (MAD) for the 7 indexed bands were <1°. Data were post-processed

120   with Oxford Instruments Channel 5.12 software suite to remove non-systematic misindexed

121   points (wild spikes) and a 6-nearest neighbors routine was used to interpolate unindexed pixels.

122

123   Atom probe and TEM specimens were prepared at Curtin University using a Tescan Lyra3 Ga^+

124   focused ion beam SEM (FIB-SEM) at Curtin University. APT specimens were mounted onto

125   prefabricated Si posts on a specimen coupon and progressively sharpened by a Ga^+ ion beam

126   using an annular milling routine. The TEM specimen was mounted on a Cu grid and thinned to

127   ~50 nm. For both APT and TEM specimens, the final stage of sample preparation involved a

128   low-voltage (2 kV) step to remove Ga implantation artefacts. Additional details of the specimen

129   preparation technique are provided in Rickard et al. (2020).

130

131   Atom probe specimens were analyzed using laser-assisted APT on the Cameca LEAP 4000X HR

132   at the Geoscience Atom Probe Facility at Curtin University. The atom probe was operated with a

133   laser pulse energy of 300 pJ, at a frequency of 200 kHz. Field evaporation was controlled by

134   maintaining a constant detection rate as voltage was steadily increased throughout the analysis.

135   Reconstructions of the time-of-flight data were undertaken using a voltage evolution model and

136   an assumed evaporation field of 32 V/nm (Saxey et al., 2019). The full acquisition and

137   reconstruction parameters are given in Supplementary Data Table A1 and a representative mass

138   spectrum is included as Fig. A1 in the Supplementary Materials. Run conditions and our

139   procedure for calculating and applying background corrections to the ^{207}Pb/^{206}Pb ratio are also

140   provided in the Supplementary Materials. Details of the APT methodology are described in

141   Reddy et al. (2020). To evaluate the trace element concentrations within nanoscale features, we

142   used Cameca's IVAS 3.8.4 software to construct proximity histograms (proxigrams; Hellman et

143   al., 2000). Proxigrams are aggregated 1-D radial histograms and were calculated using a

144   designated isoconcentration surface (0.03 at % Mg) and are measured from this surface into the

145   nanoscale features within each specimen.

146

147   TEM analyses were performed on the experimentally-heated zircon using Curtin University's

148   FEI Talos FS200X FEG TEM operated at 200 kV and equipped with a Super-X EDS detector. A

149   double tilt holder was used to tilt the sample towards the intended crystallographic zone axis.

150   The orientation was determined by navigating through the convergent beam electron diffraction

151   generated Kikuchi patterns and measuring the lattice spacing.

152

153   U and Th concentrations were measured along a transect (**Fig. 1A**) by electron probe

154   microanalysis (EPMA) on the Cameca UltraChron at the University of Massachusetts-Amherst.

155   Analyses were done at 20 kV, 400nA with a focused beam. Th and U were analyzed using the Th

156   Mα and U Mβ emission lines using large PET (LPET) and very large PET (VLPET)

157   monochromators, integrating counts from two spectrometers for each element, using a count time

158   of 730 seconds each. Background estimation was done through multipoint acquisition for Th Mα

159   and U Mβ (Allaz et al., 2019) and exponential regression; interference corrections for Th Mγ and

160   Ho Lα2 on the U Mβ emission line were applied. Matrix corrections were implemented via the

161   PAP method (Pouchou and Pichoir, 1984) and included a stoichiometric zircon composition

7

162   along with measured values of Y, Hf, and heavy rare earth elements. Analysis was performed

163   using Cameca's Peaksight interface for hardware setup (beam tuning, imaging for analysis

164   positioning), and quantitative analysis was done using Probe for EPMA software (Probe

165   Software, Inc.).

166

167   **Results**

168   Prior to annealing, portions of some zircon grains were rusty red. After annealing, rusty red

169   domains changed color to cloudy white and transparent domains remained transparent.

170

171   **SEM-CL**

172   The center of the experimentally-heated zircon grain features complexly-zoned domains that are

173   surrounded by a mottled texture (**Fig. 1**). The zircon surrounding these smaller domains is

174   characterized by fine-scale zoning; this domain is truncated by zircon that has higher contrast,

175   fine-scale CL zoning. These internal textures are all consistent with igneous processes. The grain

176   has a network of intersecting healed fractures that are dark in CL and several through-going

177   fractures. The APT specimens and TEM foil were prepared from the domain showing fine-scale

178   zoning. The untreated zircon (Fig. A2, Supplementary Materials) contains an inclusion-rich core

179   with oscillatory zoning patterns consistent with igneous growth. This grain also has a network of

180   intersecting healed fractures that are dark in CL and several intersecting, through-going fractures.

181   The APT specimen was prepared from the zircon core (see Fig. A3, Supplementary Materials).

182

183   **SEM-EBSD**

184   Crystallographic orientation data, as measured by EBSD, confirms that <001> and one of the

185   <100> axes are along the plane of the polished surface for both analyzed zircons. The <001>

186   direction is oriented parallel to the long axis of the zircon; <100> axes are perpendicular to

187   <001>, with one <100> direction oriented perpendicular to the sample surface (inset, **Fig. 1A**).

188   Neither zircon exhibit evidence of misorientation associated with crystal plasticity (Fig. A2,

189   Supplementary Materials) (Reddy et al. 2007). The APT specimens were prepared normal to the

190   polished surface (**Fig. 1B**) such that the z-axis of each atom probe specimen corresponds to the

191   <100> axis normal to the polished surface. The TEM specimen was prepared normal to the

192   polished surface and parallel to the crystallographic {100}, as shown schematically in **Fig. 1B**.

193

194   **Atom probe tomography (APT)**

195   Experimentally-treated zircon

196   Anomalously high concentrations of trace elements are found in clusters distributed throughout

197   the two atom probe specimens measured from the experimentally-treated zircon (**Fig. 2**). The

198   clusters can be classified into two categories based upon size, crystallographic orientation, and

199   composition. An isoconcentration surface of 0.03 at. % Mg was used to define the spatial extent

200   of both sets of clusters; the proxigrams show radial profiles of trace elements concentrations

201   from the isoconcentration surface into the clusters. Large clusters with a toroidal polyhedral

202   morphology (~10–25 nm diameter, 10 nm thick) are parallel to {100}, with the toroidal axis

203   oriented parallel to one of the <100> directions (**Fig. 2C**). These large clusters yield high

204   concentrations of Y, Mg, and Al (**Fig. 3**). Within the clusters, Y exceeds 6.2 at. %; Mg and Al

205   are ~ 2 at. % and preferentially aligned with <001>. Yb and Pb are above background (up to 0.5

206   at. % and 0.17 at. %), but concentrations of Ca, P, U, and Hf are not elevated within the clusters.

207 For comparison, trace element concentrations (in at. %, 1σ) in the matrix are as follows: Y =

208 0.218 ± 0.009, Mg = 0.006 ± 0.001, Al = 0.022 ± 0.003, Yb = 0.019 ± 0.001, and Pb ~$0.004 \pm$

209 0.001.

210

211 Smaller, similarly-shaped clusters (~5–15 nm diameter) are oriented parallel to {100} and {001};

212 these clusters are characterized by high concentrations of Y, Mg, and Al (**Fig. 2D, 3**). Clusters

213 with the toroidal axis oriented parallel to the z-axis of the specimen can be difficult to recognize

214 as torus-shaped features, which may be related to an evaporation effect wherein the geochemical

215 difference between the clusters and the specimen matrix leads to a local field effect and ion

216 trajectory aberrations (e.g., Fougerouse et al., 2016; Peterman et al., 2016). Y concentrations are

217 as high as 7 at. % whereas Mg and Al reach 1.5 at. %. Similar to the larger clusters, Yb and Pb

218 are above background (up to 0.5 at. %), but Ca, P, U, and Hf are not elevated within the clusters.

219

220 The background-corrected $^{207}Pb/^{206}Pb$ calculated from within the clusters is 0.264 ± 0.025 (1σ),

221 with no significant difference observed between the large and small clusters (0.302 ± 0.067 and

222 0.255 ± 0.027, respectively; both 1σ). Assuming concordance, no initial common Pb, and

223 accepted decay constants (Schoene, 2014), the calculated ratio corresponds to a crystallization

224 age of 3268 ± 150 Ma (1σ).

225

226 Untreated zircon

227 Atom probe reconstructions of a specimen prepared from the untreated zircon show that all trace

228 elements are distributed homogeneously—there is no evidence of any trace element clustering

229 (**Fig. 4**).

10

230

231 **Transmission Electron Microscopy (TEM)**

232 Bright field TEM images (**Fig. 5**) show heterogeneously-distributed, lens-shaped features, many

233 of which exhibit multiple sets of Moiré fringes that are the product of the superposition of the

234 matrix lattice over the lattice within the lens-shaped feature. The size, density, and morphology

235 of these features compare favorably with the clusters observed via APT. These features can be

236 subdivided into two dominant size distributions: 10–25 nm and 5–15 nm. The edges of these

237 features are aligned with the {100} and {001} (**Fig. 5A, B**); some edges are also aligned with

238 {101} (**Fig. 5C**). Close inspection shows that the rounded edge segments are defined by steps

239 across the lattice along the {100}, {001} and {101} planes, indicating that the features are

240 crystallographically constrained and best described as having a toroidal polyhedral morphology.

241 Compositional analysis by STEM-EDS indicates high concentrations of Al and Mg (**Fig. 5D, E**)

242 within the dislocation loops; Y concentrations are also high and Pb is below detection (0.2 at%).

243

244 **EPMA**

245 Across the region of interest in the experimentally heated grain, U concentrations range from 177

246 to 346 ppm and Th concentrations from 99 to 255 ppm. Individual spot analyses have

247 measurement uncertainties of ~4%. Because we cannot directly correlate the U and Th

248 concentrations with the atom probe specimens, we used the mean concentrations for U and Th

249 (249 ± 43 and 163 ± 43 ppm (1σ), respectively) from the domain proximal to our APT

250 specimens in our calculations. For the untreated grain, mean U is 233 ± 48 ppm (1σ) and Th is

251 116 ± 30 ppm (1σ).

252

<div align="center">**Discussion**</div>

253

254   Atom probe and TEM analyses of experimentally-heated zircon reveal two types of clusters,

255   neither of which are observed in APT specimens from the untreated zircon. Although the cluster

256   types differ with respect to composition, morphology and size, the Pb isotopic ratio extracted

257   from both types of clusters is the same, within the uncertainty of our measurements. The

258   contemporaneous formation of these cluster types merits discussion regarding the timing and

259   mechanisms of trace element segregation in zircon.

260

261   **The timing of Pb cluster formation**

262   To determine the timing of Pb clustering, we first consider the geological context. After initial

263   assembly and stabilization, the Kaapvaal craton was affected by several accretionary tectonic

264   events, the most significant of which was the Namaqua-Natal orogenic event, which spanned

265   from 1.2 to 1.0 Ga (Baughman and Flowers, 2020). If the clusters formed in response to a

266   geologic event, such as the assembly of the Kaapvaal craton ~3.0 Ga or the Namaqua-Natal

267   orogenesis and the emplacement of large igneous bodies ~1.2 Ga, the $^{207}Pb/^{206}Pb$ of the clusters

268   would have effectively ceased to evolve from the time of the geologic event because the clusters

269   contain no elevated U (Valley et al., 2015; Peterman et al., 2016, 2019; Lyon et al., 2019). At U

270   concentrations of 249 ppm, we calculate a U density of ~2 atoms U per 500 nm^3 volume (the

271   approximate size of the clusters). Given the half-lives of the ^{238}U and ^{235}U and assuming the

272   maximum interval over which U within the clusters could have decayed (3.1 Ga), these

273   concentrations would correspond to a maximum of 2 atoms of ^{206}Pb and 1 atom of ^{207}Pb that

274   could have been produced from U located within the clusters. These uncertainties are equivalent

275   to our counting statistics, so the potential contribution of Pb atoms from U trapped in the clusters

12

276   is negligible. Assuming no common Pb at the time of zircon growth and a crystallization age of

277   3.13 Ga, the modeled cluster Pb ratios are 0.569 or 0.320 for 3.0 Ga and 1.2 Ga events,

278   respectively. However, the measured $^{207}Pb/^{206}Pb$ ratios from the clusters of 0.264 ± 0.025 are

279   consistent with modern-day Pb isotopic ratios from an undisturbed 3.27 ± 0.15 Ga (1σ) zircon;

280   this date is broadly consistent with dates measured from a nearby granitoid (3.13 ± 0.06 Ga (1σ)

281   from the air-abraded grains; Schoene and Bowring, 2006). Therefore, we conclude that the

282   clustering of Pb, and the spatially associated trace elements, was produced by the laboratory-

283   induced heating of the grain for 24h at 1450°C, and there has been no nanoscale disruption to the

284   U-Pb isotopic system by geologic processes since original crystallization. These interpretations

285   are further corroborated by the absence of nanoscale features in the untreated zircon from the

286   same sample. Notably, the absence of clusters in this untreated zircon, as well as results from

287   other zircon specimens (e.g., Exertier et al., 2018; Saxey et al., 2018; Peterman et al., 2019;

288   Reddy et al., 2020) precludes sample preparation as a cause of cluster formation.

289

290   **Mechanisms of cluster formation**

291   Previous work on nanoscale trace element clustering in zircon and monazite suggest a range of

292   possible mechanisms for trace element segregation, including the production of metallic Pb

293   nanospheres via phase separation in response to UHT metamorphism (Kusiak et al., 2015;

294   Whitehouse et al., 2017), exsolution of distinct mineral inclusions during secondary processes

295   (Fougerouse et al., 2018; Seydoux-Guillaume et al., 2019), spinodal decomposition of zircon-

296   xenotime solid solution (Peterman et al., 2019), and the accumulation of trace elements in either

297   amorphous domains (Valley et al., 2014; 2015) or dislocation loops (Peterman et al., 2016; 2019)

298   in response to diffusion. Compositional analysis of the experimentally-induced clusters indicate

13

299   that the clusters are trace-element-enriched zircon, not a compositionally distinct phase (**Fig. 3**).

300   Therefore, despite the high T of our experimental heating conditions, there is no evidence for

301   phase separation to produce metallic Pb nanospheres (cf. Kusiak et al., 2015; Whitehouse et al.,

302   2017) or the exsolution of distinct mineral inclusions (Fougerouse et al., 2018, Seydoux-

303   Guillaume et al., 2019). Furthermore, Y and P do not co-vary (**Fig. 3**), which rejects the

304   possibility that these trace element clusters were produced by spinodal decomposition of zircon-

305   xenotime (Peterman et al., 2019).

306

307   The other postulated mechanism for trace element clustering is segregation to defects. Because

308   of the low diffusivity of Pb in crystalline zircon (e.g., Cherniak et al., 1991; Cherniak, 2010),

309   diffusive transport of Pb (and other trace elements) of more than a few nm under most geologic

310   conditions is greatly facilitated by significant accumulation of radiation damage (Geisler et al.,

311   2001; Ewing et al., 2003; Cherniak, 2010). Using the measured concentrations for U and Th (249

312   and 163 ppm, respectively) and the known age of crystallization, we calculate an integrated α-

313   dose of 4.4 x 10^{18} α/g, which is near the second percolation point for zircon (Murakami et al.,

314   1991; Salje et al., 1999; Ewing et al. 2003; Pidgeon, 2014). By 1.2 Ga—the timing of the

315   Namaqua-Natal orogenic event—the zircon would have accumulated most of its radiation

316   damage (3.2 x 10^{18} α/g), but large-scale structural recovery is not expected to have occurred at

317   temperatures of 200°C (Meldrum et al. 1998; Garver et al., 1999; Geisler et al. 2001; Nasdala et

318   al. 2001; 2004; Ginster et al., 2019), which is the peak temperature of the Namaqua-Natal

319   orogenic event (Baughman and Flowers, 2020).

320

14

321   In sum, these data indicate that the analyzed zircon had accumulated significant radiation

322   damage prior to our experiments, despite a low-T thermal event at ~ 1.2 Ga. Pb was mobilized

323   during laboratory heating, consistent with the high rates of Pb diffusion at our experimental

324   conditions, particularly in radiation damaged zircon (Cherniak, 2010), and confirmed by the Pb

325   isotopic ratio extracted from the clusters. These results also show that a single, high-T, short-

326   duration thermal event can lead to the formation of morphologically different clusters at the

327   nanoscale, indicating that morphology alone cannot be used to infer that multiple cluster

328   populations means multiple thermal events.

329

330   **Crystallographic controls on trace element segregation**

331   The clusters observed in APT are preferentially located in {100} and {001} and exhibit a loop-

332   like structure (**Fig. 2**). The TEM data show that these loop-like structures have Moiré fringes

333   associated with loop-parallel defects (**Fig. 5**) and high concentrations of particular trace elements

334   (**Figs. 2, 5D, 5E**). We therefore interpret these features as trace-element-enriched dislocation

335   loops. In contrast with the well-known annealing of fission tracks and other point defects at

336   relatively low temperatures (~200°C; e.g., Garver et al., 1999), the production of dislocation

337   loops requires significantly higher temperatures. Dislocation loops measuring 10–100 nm have

338   been shown to form in radiation damaged zircon in response to 24h heating experiments at

339   1250°C and 1450°C (Bursill and McLaren, 1966), which is consistent with our experiments.

340

341   We also observe a crystallographic control on the size and composition of the dislocation loops.

342   Our TEM data show that the loops lie in {100} and {001}, with the loop edges aligned with

343   {100}, {001} and {101}. The largest loops are preferentially located in {100} planes that are

344 parallel to the z-axis of the atom probe specimen. Notably, higher concentrations of Mg and Al

345 are found parallel to <001> within these larger loops (**Fig. 2C, 3**). Smaller loops found in {100}

346 and {001} contain the same trace elements, but Mg, Al, and Y are homogeneously distributed

347 and do not appear to define loop-like features (**Fig. 2D**). Mg and Al are commonly interstitial in

348 zircon (Hoskin and Ireland, 2000; Hoskin and Schaltegger, 2003) and more mobile than trace

349 elements incorporated into the zircon lattice, as demonstrated by anomalously high

350 concentrations of Mg and Al associated with Cottrell atmospheres around dislocations (Reddy et

351 al., 2016; 2020). As dislocations moved through the crystal, we suggest that mobile, interstitial

352 trace elements segregated to lower energy sites associated with dislocation loops, which were

353 being produced simultaneously. The distribution of Mg + Al in {100} planes is consistent with

354 slip along the {100} previously identified in zircon (Reddy et al., 2007). Although our results

355 differ from earlier work by Bursill and McLaren (1966), which suggested that dislocation loops

356 lie in {101} planes with Burgers vectors parallel to <101>, our findings are consistent with

357 energetically favorable slip systems in zircon (Reddy et al., 2007; Timms et al., 2012), yielding a

358 self-consistent result for the formation, composition, and distribution of dislocation loops within

359 the zircon.

360

361 **Comparison with naturally formed dislocation loops**

362 The dislocation loops observed in this study are similar in size and morphology to those

363 observed by our prior analyses of radiation damaged zircon from the Rhodope Metamorphic

364 Complex, located in eastern Greece (Peterman et al., 2016). We also observe similarities in the

365 distribution of elements within the loops. As with the Kaapvaal zircon, Pb in the Rhodope zircon

366 is concentrated into two bands and the 3-D reconstructions of the loops (cf. Supplemental

16

367   Materials, Peterman et al., 2016) show that the loops themselves are flattened and inclined with

368   respect to the z-axis of the atom probe specimen. These data are consistent with some

369   crystallographic control on the distribution of trace elements within the loops. Although we lack

370   the precise orientation of the atom probe specimen to be able to assess if the Pb-rich loops are

371   similarly aligned with {100}, results from EBSD analysis (Peterman et al., 2016) suggests that

372   this is probable, which is consistent with the results of this study.

373

374   We observe two key differences between the dislocation loops in Rhodope and Kaapvaal zircon

375   grains. First, the Rhodope loops contain high concentrations of Y + Pb, whereas the Kaapvaal

376   loops contain high concentrations of Y, Pb, Mg, Al, and Yb. In both cases, the trace elements

377   found at high concentration are interstitial and relatively incompatible in zircon. We suspect that

378   differences in composition among dislocation loops are related to the original composition of the

379   zircon, but the dataset is not yet large enough to directly test this hypothesis.

380

381   A second key difference is that a typical atom probe specimen from the core of the Rhodope

382   zircon contains fewer than five dislocation loops whereas the experimentally heated Kaapvaal

383   grain contains hundreds of loops in each APT specimen. Differences in dislocation loop density

384   may be related to: the radiation dose at the time of heating, the *P-T* conditions under which the

385   loops formed, or the rate of heating and/or structural recovery and annealing. We observe fewer

386   dislocation loops in the Rhodope zircon than the Kaapvaal grain, despite the significantly higher

387   radiation dose at the time of cluster formation (8.8 x 10^{18} α/g for Rhodope vs. 4.4 x 10^{18} α/g for

388   Kaapvaal), indicating that dislocation loop density is not directly correlated with radiation dose.

389   Instead, we suggest that the difference in dislocation loop density between the Rhodope and

390   Kaapvaal grains is a function of the amount of recrystallization that occurred prior to dislocation

391   loop formation, which is a function of the *P-T* history. Geologic storage at 700°C for 370 Myr

392   can result in complete structural recovery (Geisler et al., 2001), but storage at these conditions

393   for such an extended interval is unlikely. At lower temperatures, the zircon may partially

394   recover, but we would not expect to observe dislocation loops. In contrast, relatively short

395   duration geologic events (> 100 kya) at elevated temperature (> 900°C) would likely mobilize Pb

396   (and other incompatible trace elements) while structural recovery is ongoing, thereby

397   simultaneously producing dislocation loops. These findings suggest that the production and

398   density of dislocation loops may depend on the rate, duration, and absolute temperature of

399   geologic heating.

400

401   To explore the geologic significance of differences in cluster density, we sought additional

402   context by comparing the *P-T* histories of three additional radiation damaged zircon grains that

403   have been analyzed by APT, some of which have clusters that are similar in composition and

404   size to those observed in the Kaapvaal and Rhodope grains (**Table 1**). Two examples come from

405   the Jack Hills (Western Australia) and a third was sampled from the Grouse Creek Mountains

406   (Utah, USA). The Jack Hills zircon grains are 4.4 and 4.0 Ga; the 4.4 Ga grain has a 3.4 Ga rim

407   and the APT specimen contains hundreds of Y + Pb clusters. In contrast, the 4.0 Ga Jack Hills

408   grain does not have a younger rim and the APT specimen lacks any clusters (Valley et al., 2015).

409   The 2.5 Ga Grouse Creek grain has a young igneous rim attributed to a geologic event at 29 Ma

410   and the APT specimen from this sample contains a similar density of clusters to the 4.4 Ga Jack

411   Hills specimen (Valley et al., 2015). For comparison, the Kaapvaal specimens contain hundreds

412   of loops, and there is no geological evidence of moderate- to high-*T* annealing of the grain prior

18

413 to our laboratory experiments. The Rhodope zircon was metamorphosed during subduction to

414 UHP conditions along a relatively cold thermal gradient (Krenn et al., 2010); the younger rim

415 formed during upper amphibolite to granulite facies metamorphism following the UHP event

416 (Peterman et al., 2016; 2019). APT specimens from this grain contain a few clusters enriched in

417 trace elements.

418

419 Among the zircon specimens with high cluster densities, the Kaapvaal grain was subjected to a

420 steep dT/dt (400°C/h) and the rim-forming events for the 4.4 Ga Jack Hills and 2.5 Ga Grouse

421 were igneous and thus also high dT/dt, with no Pb loss. In contrast, dT/dt for the Rhodope grain

422 was more gradual and Pb loss was interpreted to have occurred early in the prograde history

423 (Peterman et al., 2016; 2019) because Pb is relatively mobile in radiation damaged zircon

424 (Cherniak, 2010). As temperature increased with progressive metamorphism, structural recovery

425 began, which resulted in a more crystalline zircon and fewer defects available to produce

426 dislocation loops. As a direct consequence, the zircon contains fewer dislocation loops, despite

427 the high radiation dose. Migrating Pb, enabled by increasing temperatures, was trapped in

428 dislocation loops, thereby yielding a $^{207}Pb/^{206}Pb$ model age consistent with Pb mobility at the

429 time of dislocation loop formation. These results suggest that the formation of dislocation loops

430 requires both accumulated radiation damage and high(er) temperature geologic events.

431 Importantly, dT/dt appears to play a significant role in both the density of clusters and amount of

432 Pb loss.

433

434 If the clusters in the 4.4 Ga Jack Hills grain are produced by the same processes, our model

435 suggests that they formed during the high-T geologic event that produced the 3.4 Ga rims; the

436   modeled Pb ages of the clusters and the observation of a preferred crystallographic orientation

437   for the clusters (parallel to (100) and (010); Valley et al., 2015) are consistent with this

438   interpretation. Similarly, the Grouse Creek grain is a xenocryst with a 29 Ma igneous rim; these

439   igneous processes could have thermally induced the formation of dislocation loops, which

440   trapped migrating Pb.

441

442   **Implications**

443   The segregation of incompatible trace elements to clusters has been reported in natural samples

444   of metamorphically heated zircon (Valley et al., 2014; 2015; Peterman et al., 2016; 2019).

445   However, the observation that short interval, high-*T* heating of zircon (e.g., 1450°C, 24h) can

446   produce large numbers of similar segregation features suggests that the presence of decorated

447   dislocation loops may be useful in identifying short duration, high-*T* geologic events. Such

448   events may include thermal spikes associated with melt sheets formed during impact cratering or

449   the entrapment of zircon xenocrysts in volcanic rocks.

450

451   In natural examples of trace element segregation to dislocation loops, the data indicate that these

452   features form during the prograde evolution of the metamorphosed zircon (Peterman et al., 2016)

453   and are therefore not destroyed at peak temperatures of >800°C over several million years. Once

454   formed, trace element segregations within dislocation loops are likely to serve as a durable

455   reservoir for trace element entrapment in zircon. This has potential implications for

456   understanding diffusion in zircon because diffusion out of these segregations will have a

457   fundamentally different activation energy than typical volume diffusion. In addition, the

458   segregations may continue to act as a local sink for trace elements diffusing through the zircon

459   lattice. In these cases, the behavior of trace elements within segregations may become decoupled

460   from those that are not segregated, for example Pb and Ti respectively, which may have

461   implications for deriving T-t histories from zircon at the nanoscale.

462

463   The entrapment of particular trace elements in nanoscale defects has potential minerals

464   engineering applications. Zircon has been considered as a potential repository for nuclear waste

465   materials (e.g., Ewing, 1999) because it is considered to be physically and chemically stable over

466   geological timescales. The experimental data presented here indicate that nanoscale segregations

467   of entrapped trace elements can be engineered under laboratory conditions over short timescales

468   (hours to days), even in robust minerals such as zircon. These segregations provide an additional

469   level of geochemical isolation from the environment and may prove useful in the storage of

470   noxious materials, such as nuclear waste.

471

472   **Acknowledgements**

484

References

485   Allaz, J.M., Williams, M.L., Jercinovic, M.J., Goemann, K., and Donovan, J. (2019) Multipoint

486   background analysis: Gaining precision and accuracy in microprobe trace element analysis.

487   Microscopy and Microanalysis, 25, 30-46.

488

489

490   Baughman, J.S., and Flowers, R.M. (2020) Mesoproterozoic burial of the Kaapvaal craton,

491   southern Africa during Rodinia supercontinent assembly from (U-Th)/He thermochronology.

492   Earth and Planetary Science Letters, 531, 115930, https://doi.org/10.1016/j.epsl.2019.115930

493

494   Blum, T.B., Darling, J.R., Kelly, T.F., Larson, D.J., Moser, D.E., Perez-Huerta, A., Prosa, T.J.,

495   Reddy, S.M., Reinhard, D.A., Saxey, D.W., Ulfig, R., and Valley, J.W. (2017) Best practices for

496   reporting atom probe analysis of geological materials. *In* Microstructural Geochronology:

497   Planetary Records Down to Atom Scale, 369-373.

498

499   Bursill, L.A., and McLaren, A.C. (1966) Transmission electron microscope study of natural

500   radiation damage in zircon (ZrSiO4). Physica Status Solidi B, 13, 331–343.

501

502   Cherniak, D.J., Lanford, W.A., and Ryerson, F.J. (1991) Lead diffusion in apatite and zircon

503   using ion implantation and Rutherford Backscattering techniques. Geochimica et Cosmochimica

504   Acta, 55, 1663-1673.

505

506   Cherniak, D.J., and Watson, E.B. (2003) Diffusion in zircon. In: Hanchar J.M., Hoskin P.W.O.

507   (eds) Zircon. Reviews in Mineralogy and Geochemistry, 53, 113–143.

508

509   Cherniak, D.J. (2010) Diffusion in accessory minerals: zircon, titanite, apatite, monazite and

510   xenotime. Reviews in Mineralogy and Geochemistry, 72, 827–869.

511

512   de Wit, M.J., Roering, C., Hart, R.J., Armstrong, R.A., de Ronde, C.E.J., Green, R.W.E.,

513   Tredoux, M., Peberdy, E., and Hart, R.A. (1992) Formation of an Archean continent. Nature,

514   357, 553–562.

515

516   Ewing, R.C. (1999) Nuclear waste forms for actinides. Proceedings of the National Academy

517   Sciences of the United States of America, 96, 3432-3439.

518

519   Ewing, R.C., Meldrum, A., Wang, L., Weber, W.J., and Corrales, L.R. (2003) Radiation effects

520   in zircon. In: Hanchar J.M., Hoskin P.W.O. (eds) Zircon. Reviews in Mineralogy and

521   Geochemistry, 53, 387–425.

522

523   Exertier, F., La Fontaine., A., Corcoran, C., Piazolo, S., Belousova, E., Peng, A., Gault, B.,

524   Saxey, D.W., Fougerouse, D., Reddy, S.M., Pedrazzini, S., Bagot., P.A.J., Moody, M.P.,

525   Langelier, B., Moser., D.E., Botton, G.A., Vogel, F., Thompson, G.B., Blanchard, P.T.,

526   Chiaramonti, A.N., Reinhard, D.A., Rice, K.P., Schreiber, D.K., Kruska, K., Wang, J., and

527   Cairney, J.M. (2018) Atom probe tomography analysis of the reference zircon GJ-1: An

528   interlaboratory study. Chemical Geology, 495, 27-35.

529

530   Fougerouse, D., Reddy, S.M., Saxey, D.W., Rickard, W.D.A., van Riessen, A., and

531   Micklethwaite, S. (2016) Nanoscale gold clusters in arsenopyrite controlled by growth rate not

532   concentration: evidence from atom probe microscopy. American Mineralogist, 101, 1916–1919.

533

534   Fougerouse, D., Reddy, S.M., Saxey, D.W., Erickson, T.M., Kirkland, C.L., Rickard, W.D.A.,

535   Seydoux-Guillaume, A.M., Clark C., and Buick, I.S. (2018) Nanoscale distribution of Pb in

536   monazite revealed by atom probe microscopy. Chemical Geology, 479, 251–258

537

538   Garver, J.I., Brandon, M.T., Roden-Tice, M.K., and Kamp, P.J.J. (1999) Exhumation history of

539   orogenic highlands determined by detrital fission track thermochronology. *In* Ring, U., Brandon,

540   M.T., Willet, S.D., and Lister, G.S. (eds) Exhumation processes: normal faulting, ductile flow.

541   Geological Society of London Special Publications, 154, 283-304.

542

543   Ge, R., Wilde, S.A., Nemchin, A.A., Whitehouse, M.J., Bellucci, J.J., Erickson, T.M., Frew, A.,

544   and Thern, E.R. (2018) A 4463 Ma apparent zircon age from the Jack Hills (Western Australia)

545   resulting from ancient Pb mobilization. Geology, 46, 303-306.

546

547   Geisler, T., Pidgeon, R.T., van Bronswijk, W., and Pleysier, R. (2001) Kinetics of thermal

548   recovery and recrystallization of partially metamict zircon: a Raman spectroscopic study.

549   European Journal of Mineralogy, 13, 1163-1176.

550

551   Geisler, T. (2002) Isothermal annealing of partially metamict zircon: evidence for a three-stage

552   recovery process. Physics and Chemistry of Minerals, 29, 420–429.

553

554   Geisler, T., Schaltegger, U., and Tomaschek, F. (2007) Re-equilibration of zircon in aqueous

555   fluids and melts. Elements, 3, 43–50.

556

557   Ginster, U., Reiners, P.W., Nasdala, L., and Chanmuang N., C. (2019) Annealing kinetics of

558   radiation damage in zircon. Geochimica et Cosmochimica Acta, 249, 225-246.

559

560   Harley, S.L., Kelly, N.M., and Möller, A. (2007) Zircon behaviour and the thermal histories of

561   mountain chains. Elements, 3, 25–30.

562

563   Hazen, R.M., and Finger, L.W., 1979. Crystal structure and compressibility of zircon at high

564   pressure. American Mineralogist, 64, 196-201.

565

566   Hellman, O.C., Vandenbroucke, J.A., Rüsing, J., Isheim, D., and Seidman, D.N. (2000) Analysis

567   of Three-dimensional Atom-probe Data by the Proximity Histogram. Microscopy and

568   Microanalysis, 6, 437–444.

569

570   Hoskin, P.W.O., and Ireland, T.R. (2000) Rare earth element chemistry of zircon and its use as a

571   provenance indicator. Geology, 28, 627–630.

572

573   Hoskin, P.W.O., and Schaltegger, U. (2003) The composition of zircon and igneous and

574   metamorphic petrogenesis. In: Hanchar J.M., Hoskin P.W.O. (eds) Zircon. Reviews in

575   Mineralogy and Geochemistry, 53, 27–62.

576

577 Krenn, K., Bauer, C., Proyer, A., Klötzli, U., and Hoinkes, G. (2010) Tectonometamorphic

578 evolution of the Rhodope orogen. Tectonics, 29, TC4001 https://doi.org/10.1029/2009TC002513

579

580 Kusiak, M.A., Whitehouse, M.J., Wilde, S.A., Nemchin, A.A., and Clark C. (2013) Mobilization

581 of radiogenic Pb in zircon revealed by ion imaging: Implications for early Earth geochronology.

582 Geology, 41, 291-294.

583

584 Kusiak, M.A., Dunkley, D.J., Wirth, R., Whitehouse, M.J., Wilde, S.A., and Marquardt, K.

585 (2015) Metallic lead nanospheres discovered in ancient zircons. Proceedings of the National

586 Academy of Sciences, 112, 4958-4963.

587

588 Layer, P.W., Kroner, A., and York, D. (1992) Pre-3000 Ma thermal history of the Archean Kaap

589 valley pluton, South Africa. Geology, 20, 717–720.

590

591 Lyon, I.C., Kusiak, M.A., Wirth, R., Whitehouse, M.J., Dunkley, D.J., Wilde, S.A., Schaunlöffel,

592 D., Malherbe, J., and Moore, K.L. (2019) Pb nanospheres in ancient zircon yield model ages for

593 zircon formation and Pb mobilization. Nature, 9, 13702. https://doi.org/10.1038/s41598-019-

594 49882-8

595

596 Meldrum, A., Boatner, L.A., Weber, W.J., and Ewing, R.C. (1998) Radiation damage in zircon

597 and monazite. Geochimica et Cosmochimica Acta, 62, 2509–2520.

598

599   Montalvo, S.D., Reddy, S.M., Saxey, D.W., Rickard, W.D.A., Fougerouse, D., Quadir, Z., and

600   Johnson, T.E. (2019) Nanoscale constraints on the shock-induced transformation of zircon to

601   reidite. Chemical Geology, 507, 85-95.

602

603   Murakami, T., Chakoumakos, B.C., Ewing, R.C., Lumpkin, G.R., and Weber, W.J. (1991)

604   Alpha-decay event damage in zircon. American Mineralogist, 76, 1510-1532.

605

606   Nasdala, L., Wenzel, M., Vavr, G., Irmer, G., Wenzel, T., and Kober, B. (2001) Metamictization

607   of natural zircon: accumulation versus thermal annealing of radioactivity-induced damage.

608   Contributions to Mineralogy and Petrology, 141, 125-144.

609

610   Nasdala, L., Lengauer, C.L., Hanchar, J.M., Kronz, A., Wirth, R., Blanc, P., Kennedy, A.K., and

611   Seydoux-Guillaume, A-M. (2002) Annealing radiation damage and the recovery of

612   cathodoluminescence. Chemical Geology, 191, 121-140.

613

614   Nasdala, L., Reiners, P.W., Garver, J.I., Kennedy, A.K., Stern, R.A., Balan, E., and Wirth, R.

615   (2004) Incomplete retention of radiation damage in zircon from Sri Lanka. American

616   Mineralogist, 89, 219-231.

617

618   Peterman, E.M., Reddy, S.M, Saxey, D.W., Snoeyenbos, D.R., Rickard, W.D.A., Fougerouse,

619   D., and Kylander-Clark, A.R.C. (2016) Nanogeochronology of discordant zircon measured by

620   atom probe microscopy of Pb-enriched dislocation loops. Science Advances, 2, e:1601218. doi:

621   10.1126/sciadv.1601318

622

623   Peterman, E.M., Reddy, S.M, Saxey, D.W., Fougerouse, D., Snoeyenbos, D.R., and Rickard,

624   W.D.A. (2019) Nanoscale processes of trace element mobility in metamorphosed zircon.

625   Contributions to Mineralogy and Petrology, 174, 92. https://doi.org/10.1007/s00410-019-1631-1

626

627   Piazolo, S., La Fontaine, A., Trimby, P., Harley, S., Yang, L., Armstrong, R., and Cairney, J.M.

628   (2016) Deformation-induced trace element redistribution in zircon revealed using atom probe

629   tomography. Nature Communications, 7, 10490. https://doi.org/10.1038/ncomms10490

630

631   Pidgeon, R.T. (2014) Zircon radiation damage ages. Chemical Geology, 367, 13-22.

632

633   Pouchou, J.-L. and Pichoir, F. (1984) A new model for quantitative X-ray

634   microanalysis. 1. Application to the analysis of homogeneous samples. La Recherche

635   Aerospatiale, 3, 167-192.

636

637   Reddy, S.M., Timms, N.E., Pantleon, W., and Trimby, P. (2007) Quantitative characterization of

638   plastic deformation of zircon and geologic implications. Contributions to Mineralogy and

639   Petrology, 153, 625-645.

640

641   Reddy, S.M., van Riessen, A., Saxey, D.W., Johnson, T.E., Rickard, W.D.A., Fougerouse, D.,

642   Fischer, S., Prosa, T.J., Rice, K.P., Reinhard, D.A., Chen, Y., and Olson, D. (2016) Mechanisms

643   of deformation-induced trace element migration in zircon resolved by atom probe and correlative

644   microscopy. Geochimica et Cosmochimica Acta, 195, 158-170.

645

646   Reddy, S.M., Saxey, D.W. Rickard, W.D.A., Fougerouse, D., Montalvo, S.D., Verberne, R., and

647   van Riessen A. (2020) Atom Probe Tomography: Development and Application to the

648   Geosciences. Geostandards and Geoanalytical Research, 44, 5-50.

649

650   Rickard, W.D.A., Reddy, S.M., Saxey, D.W., Fougerouse, D., Timms, N.E., Daly, L., Peterman,

651   E., Cavosie, A.J., and Jourdan F. (2020) Novel Applications of FIB-SEM-Based ToF-SIMS in

652   Atom Probe Tomography Workflows. Microscopy and Microanalysis, 26, 750-757.

653

654   Rubatto, D. (2002) Zircon trace element geochemistry: Partitioning with garnet and the link

655   between U–Pb ages and metamorphism. Chemical Geology, 184, 123–138.

656

657   Salje, E.K.H., Chrosch, J., and Ewing, R.C. (1999) Is "metamictization" of zircon a phase

658   transition?. American Mineralogist, 84, 1107-1116.

659

660   Saxey, D.W., Reddy, S.M., Fougerouse, D., and Rickard, W.D.A. (2018) The Optimization of

661   Zircon Analyses by Laser-Assisted Atom Probe Microscopy: Insights from the 91500 Zircon

662   Standard. *In Mi*crostructural Geochronology: Planetary Records Down to Atom Scale, 293–313.

663

664   Saxey, D., Fougerouse, D., Rickard, W., and Reddy, S. (2019) Spatial Reconstruction of Atom

665   Probe Data from Zircon. Microscopy and Microanalysis, 25, 2536-2537.

666

667   Schoene, B., and Bowring, S.A. (2006) Determining accurate temperature–time paths from U–Pb

668   thermochronology: An example from the Kaapvaal craton, southern Africa. Geochimica et

669   Cosmochimica Acta, 71, 165-185.

670

671   Schoene, B. (2014) U-Th-Pb geochronology. In Rudnick, R. (Ed.). Treatise on Geochemistry,

672   4.10, 341-378.

673

674   Seydoux-Guillaume, A.-M., Fougerouse, D., Laurent, A., Gardés, E., Reddy, S., and Saxey, D.

675   (2019) Nanoscale resetting of the Th/Pb system in an isotopically-closed monazite grain: A

676   combined atom probe and transmission electron microscopy study. Geoscience Frontiers, 10, 65-

677   76.

678

679   Timms, N.E., Reddy, S.M., Healy, D., Nemchin, A.A., Grance, M.L., Pidgeon, R.T., and Hart,

680   R. (2012) Resolution of impact-related microstructures in lunar zircon: A shock-deformation

681   mechanism map. Meteoritics and Planetary Science, 47, 120-141.

682

683   Valley, J.W., Cavosie, A.J., Ushikubo, T., Reinhard, D.A., Lawrence, D.F., Larson, D.J., Clifton,

684   P.H., Kelly, T.F., Wilde, S.A., Moser, D.E., and Spicuzza, M.J. (2014) Hadean age for a post-

685   magma-ocean zircon confirmed by atom-probe tomography. Nature Geoscience, 7, 219–223.

686

687   Valley, J.W., Reinhard, D.A., Cavosie, A.J., Ushikubo, T., Lawrence, D.F., Larson, D.J., Kelly,

688   T.F., Snoeyenbos, DR., and Strickland, A. (2015) Nano-and micro-geochronology in Hadean and

689   Archean zircons by atom-probe tomography and SIMS: New tools for old minerals. American

690   Mineralogist, 100, 1355-1377.

691

692   Whitehouse, M.J., Kusiak. M.A., Wirth. R., and Ravindra Kumar, G.R. (2017) Metallic Pb

693   nanospheres in ultra-high temperature metamorphosed zircon from southern India. Mineralogy

694   and Petrology, 111, 467-474.

695

Figure Captions

696
697

698   **Figure 1.** A) Cathodoluminescence (CL) image of the analyzed zircon. Yellow box marks

699   location of TEM foil; white box marks lift out location for atom probe specimens. Cyan dots

700   mark the EPMA transect; box outlines the points used to determine U and Th concentrations.

701   Pole figure shows the <100> and <001> of this grain, as measured by EBSD. B) Schematic

702   diagram of zircon with relevant crystallographic axes and planes marked; APT specimens

703   (orange) and TEM foil (yellow) shown in their crystallographic context.

704

705   **Figure 2.** Atom probe tomography reconstructions from the experimentally heated zircon. Each

706   point represents an atom; colors reflect different elements. A) Whole specimen, multiple

707   elements. B) Single element reconstructions. C & D) Close-up images of representative clusters.

708   C is in the x- z plane of the specimen; D is in the x-y plane of the specimen.

709

710   **Figure 3.** Proxigram shows changes in concentration (at. %) with respect to the edge of the

711   cluster in nm. Clusters were defined by an isoconcentration surface of 0.03 at. % Mg.

712

713   **Figure 4.** Atom probe tomography reconstructions from the untreated zircon. Each point

714   represents an atom; colors reflect different elements. Crystallographic directions and specimen

715   orientations as marked. Pb (green) is shown with Si (gray).

716

717   **Figure 5.** Bright field TEM images show the size and distribution of dislocation loops within the

718   analyzed zircon. *Inset*: diffraction pattern with <001> and <100> identified; all images were

719   collected in the same orientation. (A) White arrows mark strained regions of the lattice; black

720   arrow indicates Moiré fringes. The edges of the loop in (B) are aligned with {100} and {001};

721   these planes are shown by white dashed lines. The edges of the loop in (C) are aligned with

722   {101} (shown by yellow dotted lines), {100} and {001}. Compositional maps acquired via

723   STEM-EDS of Al (D) and Mg (E) within dislocation loops; maps were collected from an area

724   adjacent to the region shown in A.

725   **Table 1: Attributes of zircons analyzed by APT**

	Rhodope[1]	Kaapvaal	Jack Hills 4.4[2]	Jack Hills 4.0[2]	Grouse Creek[2]
Crystallization age	2144 ± 33 Ma	3268 ± 150 Ma	4374 ± 6 Ma	4007 ± 22 Ma	2542 ± 5 Ma
Cluster density	Low	High	High	None	High
% concordance of zircon core	66	n.d.	100	97	97
Rim age	180 – 150 Ma	n/a	3400 Ma	n/a	29 Ma
α/g at time of rim formation	8.1×10^{18}	4.4×10^{18}	[3] Estimated at 1.83×10^{18}	n/a	8.05×10^{18}
Origin and dT/dt of second event	Metamorphic; low dT/dt	Laboratory; high dT/dt	Igneous; high dT/dt	n/a	Igneous; high dT/dt

726   [1] Peterman et al., 2016; [2] Valley et al., 2015; [3] Estimated based on approximate U and Th

727   concentrations (145 ppm and 100 ppm, respectively) and ages of geologic events reported in

728   Valley et al. (2015).

729   n.d. – not determined; n/a – not applicable

730

731

732 **Supplementary Materials – Analytical Run Conditions**

733 Analytical run conditions for both specimens are provided in the table below, after Blum et al.

734 (2017).

735 Supplementary Table A1: Atom Probe Tomography Data Acquisition Settings and Data Summary

Specimen	M1	M2	M13
Instrument model	LEAP 4000X HR	LEAP 4000X HR	LEAP 4000X HR
Laser wavelength (nm)	355	355	355
Laser pulse energy (pJ)	300	300	300
Pulse frequency (kHz)	200	200	200
Evaporation control	Detection rate	Detection rate	Detection rate
Target detection rate (ions/pulse)	0.01	0.01	0.01
Nominal flight path (mm)	382	382	382
Set point temperature (K)	60	60	60
Sample temperature (K)	69.2	69.2	69.2
Chamber pressure (Torr)	3.1×10^{-11}	3.3×10^{-11}	2.9×10^{-11}
Data Summary			
LAS Root version	15.41.3421	15.41.3421	15.41.3421
CAMECAROOT Version	18.46.452d	18.46.452d	18.46.452d
Analysis software	IVAS 3.8.4sp1	IVAS 3.8.4sp1	IVAS 3.8.4sp1
Total ions (millions):	56.9	100.0	77.8
Single (%)	70.6	71.0	69.5
Multiple (%)	29.2	28.8	30.2
Partial (%)	0.2	0.2	0.3
Reconstructed ions (millions) (complete dataset):	55.2	98.2	76.3
Ranged (%)	89.2	83.2	84.7
Unranged (%)	10.8	16.8	15.3
Volt./bowl corr. peak (Da)	16	16	16

Mass calibration (peaks/interp.)	8/Linear	10/Linear	10/Linear
$(M/\Delta M)$ for $^{16}O^+$	951	979	949
Time-dependent background (ppm/ns)	16.8	17.1	25.0
Reconstruction			
Final specimen state	Fractured	Intact	Intact
Pre-/post-analysis imaging	SEM/SEM	SEM/SEM	SEM/SEM
Radius evolution model	Voltage evolution	Voltage evolution	Voltage evolution
Field factor (k)	3.3	3.3	3.3
Image compression factor	1.65	1.65	1.65
Assumed E-field (V/nm)	28	28	28
Detector Efficiency (%)	36	36	36
Average atomic volume (nm^3)	0.01076	0.01076	0.01076
$V_{initial}$ (V)	4866	5456	4547
V_{final} (V)	8135	10252	8880

736   ΔM is full width at half maximum

737

738   **Pb isotopic ratio calculations and corrections**

739   The $^{207}Pb/^{206}Pb$ ratio was determined from the Pb^{++} ion peaks located in the time-of-flight mass

740   spectrum at 103 and 103.5 Da. Equivalent proportions of each peak were measured by selecting

741   the counts in a central 0.1 Da mass range. Count values were then corrected for the local

742   background noise using an estimate of the background between 100.5 and 102.5 Da, where there

743   are assumed to be no mass peaks. A further correction was applied to the ^{207}Pb signal to account

744   for an overlap between the 103.5 Da peak ($^{207}Pb^{++}$) and the extended leading-edge of the 104 Da

745   peak ($^{28}Si_2^{16}O_3^{++}$). The degree of this overlap was estimated by examining the spectrum from the

746   entire dataset (M2), in which the contribution of leading-edge counts in the 103.5 Da peak range

747   was found to be 20% of those found centered in the 104 Da peak. This correction further reduced

748   the ^{207}Pb counts, resulting in a lower ^{207}Pb/^{206}Pb ratio than would otherwise be measured.
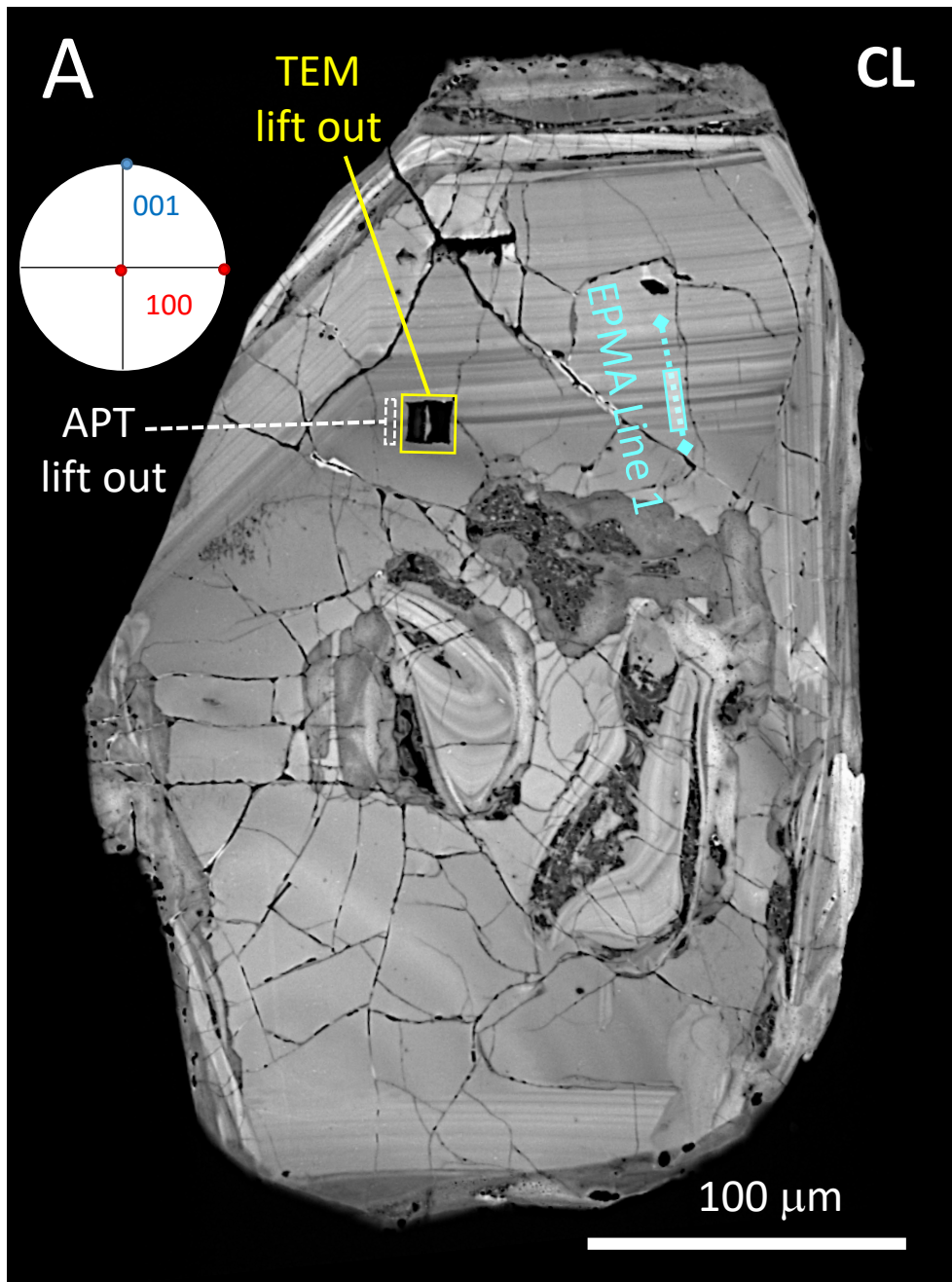
Figure 1. A) Cathodoluminescence (CL) image of the analyzed zircon. Yellow box marks location of TEM foil; white box marks lift out location for atom probe specimens. Cyan dots mark the EPMA transect; box outlines points used to determine U and Th concentrations. Pole figure shows the <100> and <001> of this grain, as measured by EBSD. B) Schematic diagram of zircon with relevant crystallographic axes and planes marked; APT specimens (orange) and TEM foil (yellow) shown in their crystallographic context.
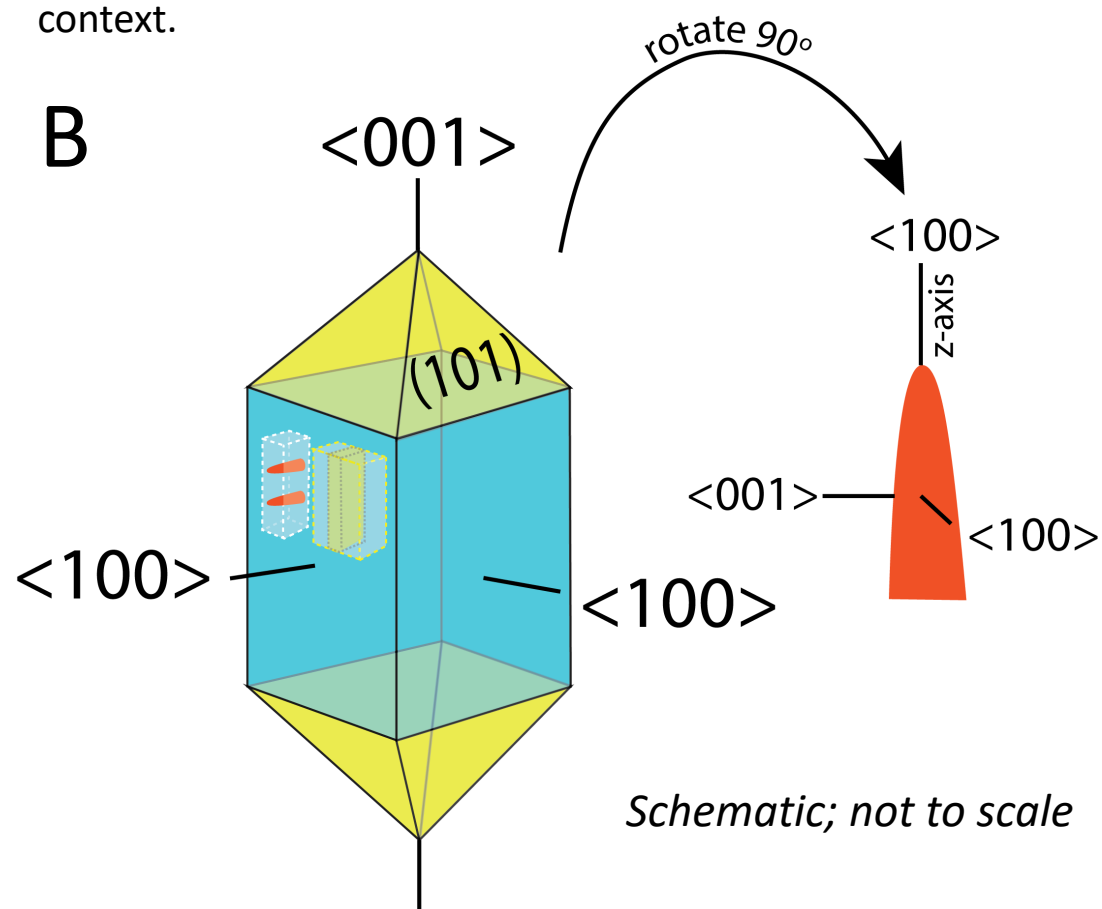
Figure 2. Atom probe tomography reconstructions from the experimentally treated zircon. Each point represents an atom; colors reflect different elements. A) Whole specimen, multiple elements. B) Single element reconstructions. C & D) Close-up images of representative clusters. C is in the x-z plane of the specimen; D is in the x-y plane of the specimen.
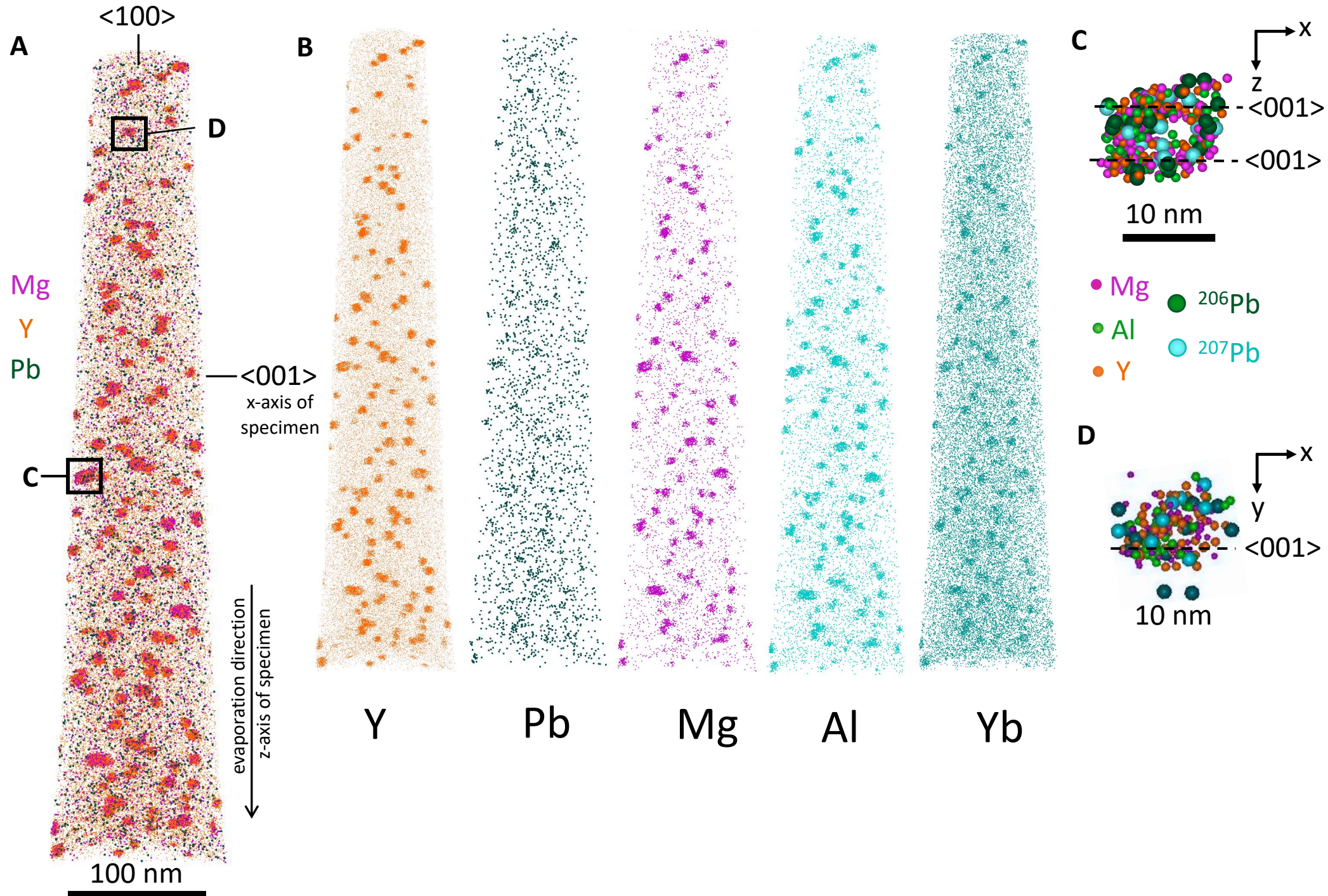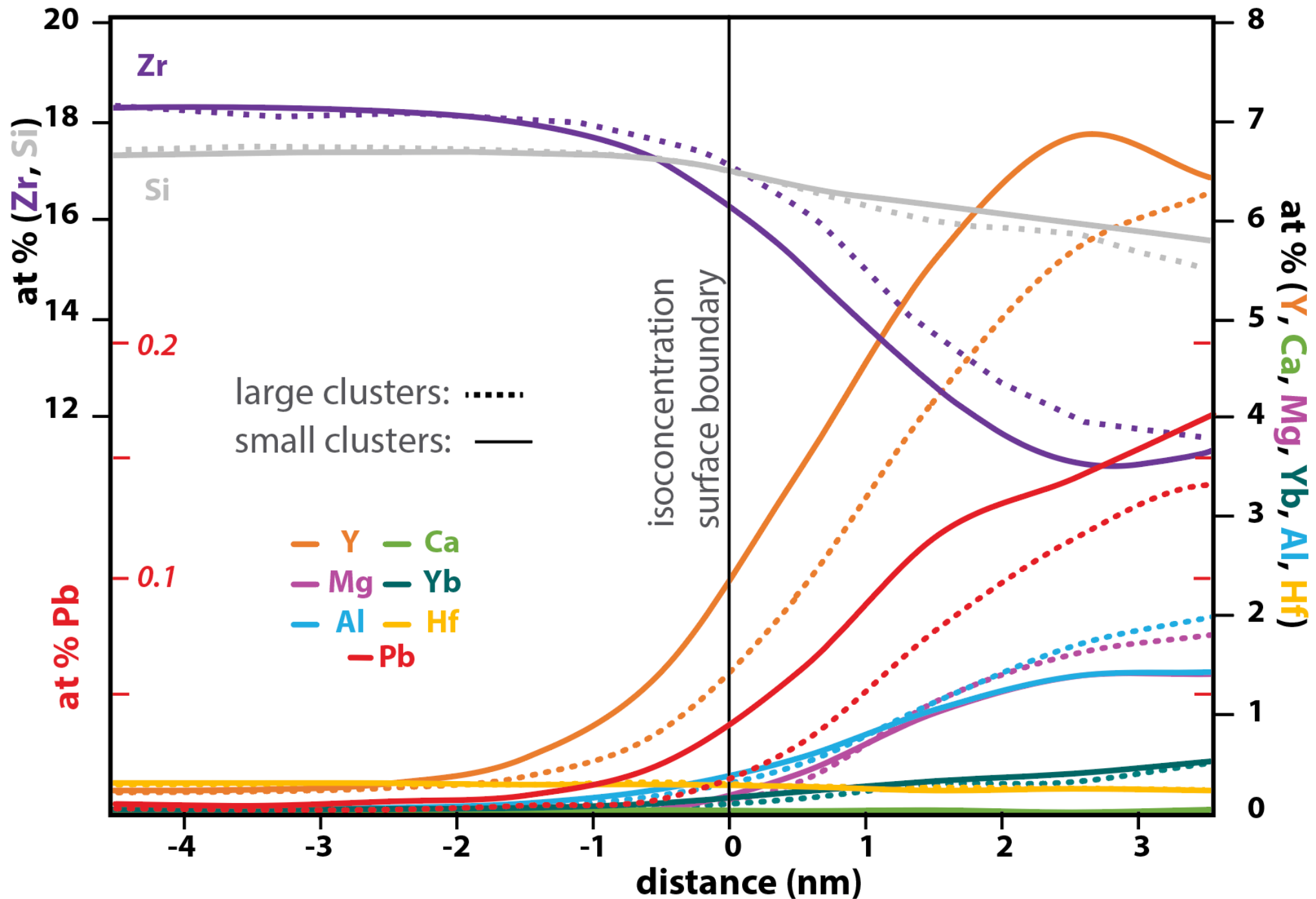
Figure 3. Proxigram shows changes in concentration (at %) with respect to the edge of the cluster in nm. Clusters were defined by an isoconcentration surface of 0.03 at. % Mg.
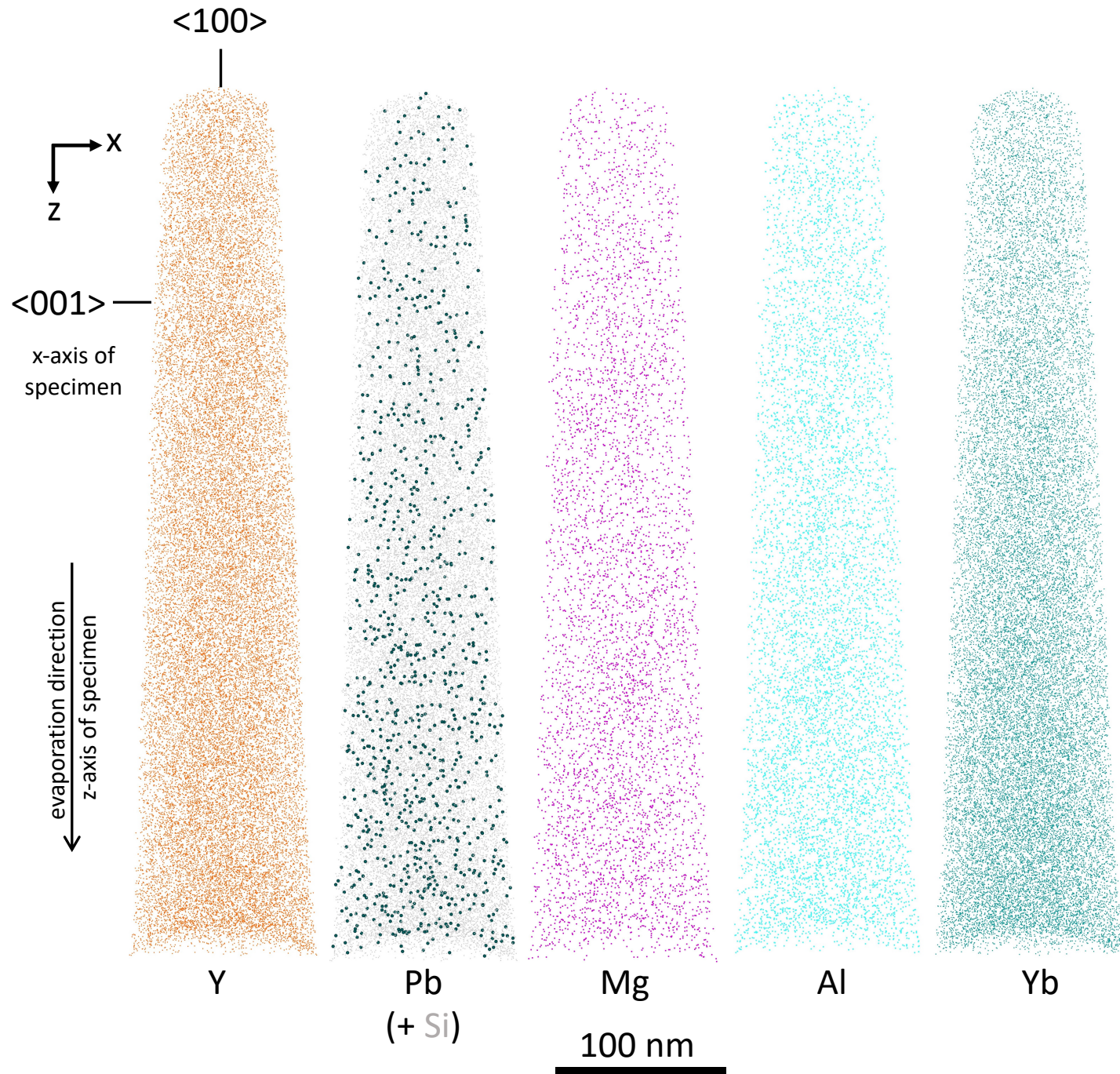
Figure 4. Atom probe tomography reconstructions from the untreated zircon. Each point represents an atom; colors reflect different elements. Crystallographic directions and specimen orientations as marked. Pb (green) is shown with Si (in gray).
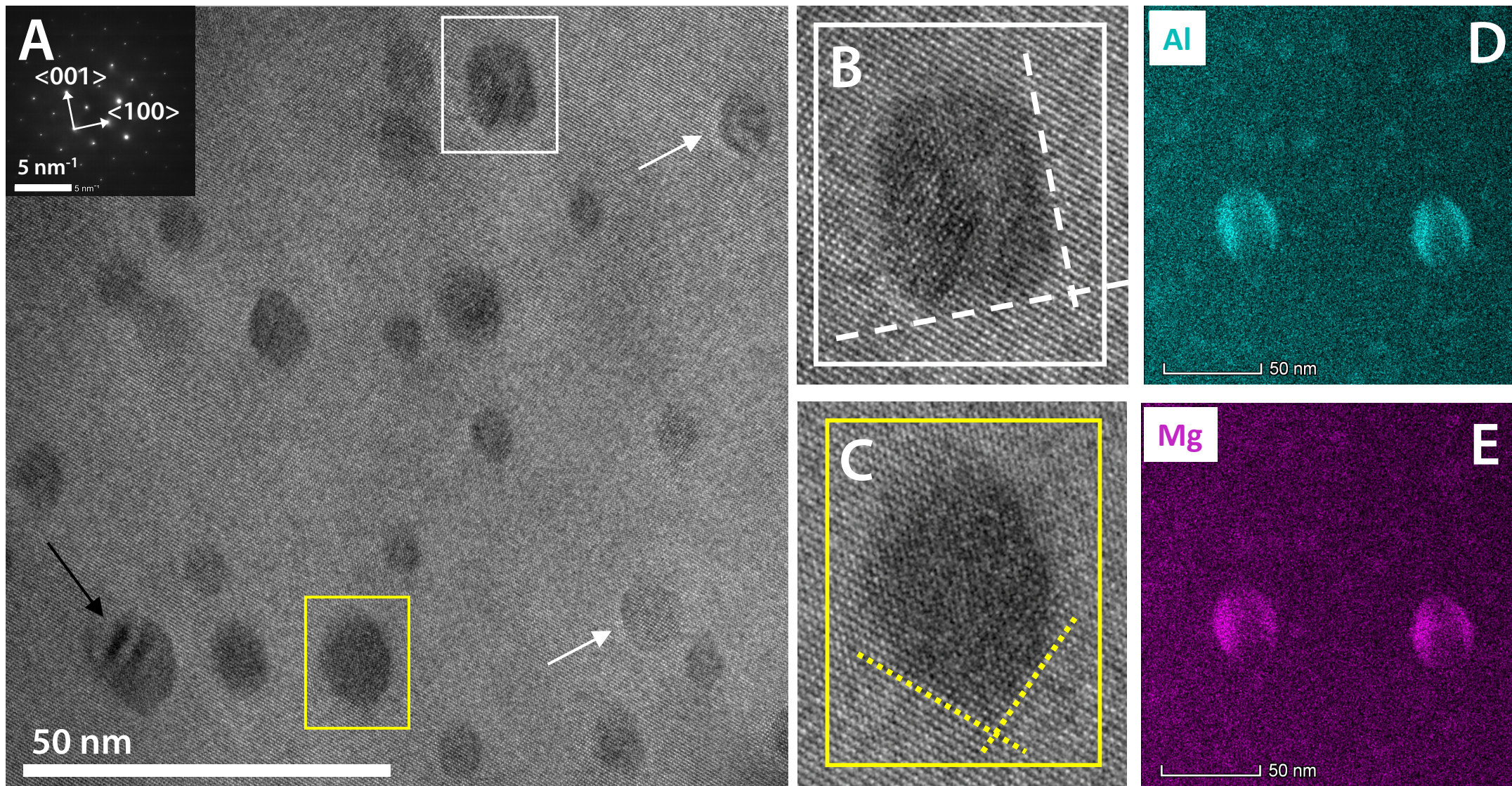
Figure 5. Bright field TEM images show the size and distribution of dislocation loops within the analyzed zircon. *Inset*: diffraction pattern with <001> and <100> identified; all images were collected in the same orientation. (A) White arrows mark strained regions of the lattice; black arrow indicates Moiré fringes. The edges of the loop in (B) are aligned with {100} and {001}; these planes are shown by white dashed lines. The edges of the loop in (C) are aligned with {101} (shown by yellow dotted lines), {100} and {001}. Compositional maps acquired via STEM EDS of Al (D) and Mg (E) within dislocation loops; maps were collected from an area adjacent to the region shown in A.